JOURNAL OF THERMOPHYSICS AND HEAT TRANSFER
Vol. 12, No. 4, October–December 1998

Numerical Solution of the Ideal Magnetohydrodynamic Equations for a Supersonic Channel Flow

Shigeki Harada,* Klaus A. Hoffmann,† and Justin Augustinus*
Wichita State University, Wichita, Kansas 67260-0044

A fourth-order modified Runge–Kutta scheme augmented with total variation diminishing (TVD) models have been developed to solve the two-dimensional magnetohydrodynamic equations for supersonic flows. Several limiters for each TVD model have been extensively investigated. The numerical scheme is proven to be accurate with the ability to capture strong shocks, expansion waves, reflective waves, and other physical phenomena occurring in the flowfield without any or with minimum oscillations in the solution. The numerical scheme has been formulated in generalized coordinates and is applied to a supersonic flow within a channel including compression and expansion corners. The effect of magnetic field on the flowfield has been investigated with the application of several externally applied magnetic fields. The solutions indicate changes in the wave strength and the formation of secondary waves.

Nomenclature

B_x, B_y, B_z = magnetic field components in the x, y, and z directions
c_s = speed of sound
$\boldsymbol{E}$, $\boldsymbol{F}$ = flux vectors components in the x and y directions
e_t = total energy per unit mass
J = Jacobian of transformation
p = pressure
$\boldsymbol{Q}$ = field vector
U, V = contravarient velocity components
u, v, w = velocity components in the x, y, and z directions
v_{ax}, v_{ay} = Alfven wave velocity in the x and y directions
x, y = Cartesian coordinates
γ = ratio of specific heats
λ = eigenvalue
ξ, η = generalized coordinates
ρ = density
$\bar{\Phi}$, $\bar{\Theta}$ = flux limiter function vectors associated with A and B

Subscripts
a = Alfven wave
f = fast wave
s = slow wave

Introduction

SEVERAL principal applications in space physics, astrophysics, electrical, nuclear, and aerospace engineering involve the interaction of fluid dynamics and magnetic fields. For example, the flow around a hypersonic vehicle upon reentry will dissociate and ionize because of high temperatures created by the bow shock around the vehicle. The ionized plasma and its interaction with the magnetic field, either self-generated or externally applied, must be considered in the design of heat shield, flight controls, and communication apparatus. Similarly, solar activities occur in regions with a strong magnetic field and any analysis must include the fluid dynamic–magnetic field interaction.

The governing equations for magnetohydrodynamic (MHD) that describe the flow of electrically conducting fluid in the presence of a magnetic field include the conservation laws of fluid dynamics augmented by terms to include magnetic field effects and the Maxwell's equation of electrodynamics.

The MHD equations are reduced to the ideal MHD equations by neglecting the dissipation terms; therefore, the flow is assumed to be nonthermally conducting and inviscid with no electrostatic force, displacement current, and resistivity. The resulting ideal MHD equations are classified as a hyperbolic system of equations.

In the past several decades computational schemes have been developed to numerically solve hyperbolic equations. Schemes introduced by Godunov[1] and Roe[2] are well known. However, most of these schemes at the earlier stages of development were first-order and, therefore, they produced a larger dissipation error that had the tendency to smear sharp flow gradients. As a result, higher-order schemes had to be developed that produced less dissipation and had a higher order of accuracy. However, some of these higher-order schemes based on central-difference approximation cause oscillations near sharp flow gradients. To alleviate/reduce the undesirable oscillations, several methods were developed. The addition of second- or fourth-order damping terms is considered as one of the techniques. Recently, a class of schemes known as total variation diminishing (TVD) was introduced.[3] Analysis of simple hyperbolic equations has shown that upwind schemes possess a low dissipation error. To extend the concept of upwind schemes to a system of hyperbolic equations, several flux vector splitting schemes have been introduced. The flux vector splitting of Steger and Warming[4] and van Leer[5] are examples of such schemes. Liou and Steffen[6] introduced a flux splitting scheme known as the advection upstream splitting method (AUSM) that splits the flux into the convective and pressure terms and possesses the advantages of both flux-vector and flux-difference splittings. Halt and Agarwal[7] introduced a scheme similar to AUSM known as the wave/particle split (WPS). The difference between the AUSM and WPS methods is the way the flux vector is split into two parts.

The numerical schemes reviewed in the preceding text have been used successfully for the solution of the Euler equations. The extension of these schemes for the solution of the MHD equations has not received adequate attention. Brio and Wu[8] developed an upwind-differencing scheme by using Roe's linearization process. Dai and Woodward introduced Godunov-

Received July 21, 1997; revision received April 16, 1998; accepted for publication April 30, 1998.

*Graduate Research Assistant, Department of Aerospace Engineering. Student Member AIAA.

†Associate Professor, Department of Aerospace Engineering. E-mail: hoffmann@ae.twsu.edu. Associate Fellow AIAA.

type schemes such as an approximate Riemann solver,[9] the piecewise parabolic method,[10] and a simple Riemann solver and high-order Godunov schemes.[11] Zachary and Colella[12] also introduced a high-order Godunov method. They introduced a simpler method to calculate the eigenvectors by introducing the primitive variables vector $\boldsymbol{W}$ and have provided the eigenvalues and eigenvectors. These schemes just discussed have been used for the one-dimensional seven-wave system of equations.

The purpose of the present work is to develop the numerical schemes for the ideal MHD equations. The modified Runge–Kutta scheme has been selected as the basic numerical scheme for the solution of the MHD equations. As is well known, the Runge–Kutta scheme using central-difference approximation possesses a dispersion error that degrades the solution for domains with sharp flow gradients, such as shock waves. Therefore, a postprocessor that provides a way to add artificial dissipation mechanisms is added to overcome this problem. TVD limiters are considered as one of these artificial dissipation mechanisms, as discussed previously. This scheme has been employed for solving Euler equations and has been extensively validated. However, the extension of the scheme to solve the MHD equations is not straightforward. One of the difficulties is the determination of the eigenvalues and eigenvectors of the system that is necessary for the implementation of TVD limiters. Furthermore, the Jacobian matrices for the eight-wave MHD possess singularity. Therefore, a procedure to remove the singularity has to be developed. Powell et al.[13] developed a new set of the governing ideal MHD equations that can be used to solve multidimensional problems. In the new set of governing equations, Powell introduced a new eigenvalue u (an eighth wave) that he calls the "magnetic divergence wave." The new eight-wave system has a source term that is proportional to $\nabla \cdot \boldsymbol{B}$.

Ideal MHD Equations

The MHD equations represent the flow of an electrically conducting fluid in a magnetic field. The system of equations is composed of conservations of mass, momentum, and energy and the Maxwell's equation of electrodynamics. The ideal MHD equations are as follows.

Conservation of mass:

$$\frac{\partial \rho}{\partial t} + \nabla \cdot (\rho \boldsymbol{V}) = 0 \tag{1}$$

Conservation of momentum:

$$\frac{\partial (\rho \boldsymbol{V})}{\partial t} + \nabla \cdot \left[\rho \boldsymbol{V}\boldsymbol{V} + \ddot{I}\left(p + \frac{\boldsymbol{B}\cdot\boldsymbol{B}}{2} \right) - \boldsymbol{B}\boldsymbol{B} \right] = 0 \tag{2}$$

Maxwell's equation of electrodynamics:

$$\frac{\partial \boldsymbol{B}}{\partial t} + \nabla \cdot (\boldsymbol{V}\boldsymbol{B} - \boldsymbol{B}\boldsymbol{V}) = 0 \tag{3}$$

and conservation of energy

$$\frac{\partial (\rho e_t)}{\partial t} + \nabla \cdot \left[\left(\rho e_t + p + \frac{\boldsymbol{B}\cdot\boldsymbol{B}}{2} \right) \boldsymbol{V} - \boldsymbol{B}(\boldsymbol{V}\cdot\boldsymbol{B}) \right] = 0 \tag{4}$$

where

$$\ddot{I} = \boldsymbol{i}\boldsymbol{i} + \boldsymbol{i}\boldsymbol{i} + \boldsymbol{k}\boldsymbol{k} \tag{5}$$

$$\boldsymbol{V} = u\boldsymbol{i} + v\boldsymbol{i} + w\boldsymbol{k} \tag{6}$$

$$\boldsymbol{B} = \frac{B_x}{\sqrt{4\pi}}\boldsymbol{i} + \frac{B_y}{\sqrt{4\pi}}\boldsymbol{i} + \frac{B_z}{\sqrt{4\pi}}\boldsymbol{k} \tag{7}$$

$$e_t = \frac{1}{2}\boldsymbol{V}\cdot\boldsymbol{V} + \frac{p}{\rho(\gamma - 1)} + \frac{\boldsymbol{B}\cdot\boldsymbol{B}}{2\rho} \tag{8}$$

The vector $\boldsymbol{B}$ is the magnetic field, p is the static pressure, whereas $\boldsymbol{B}\cdot\boldsymbol{B}/2$ is the magnetic pressure. In addition to Eqs. (1–4), the requirement of $\nabla \cdot \boldsymbol{B} = 0$ must be enforced at the initial time level and subsequent time levels.

Two-Dimensional Ideal MHD Equations

The system of the two-dimensional eight-wave equations in a flux-vector formulation can be written as

$$\frac{\partial \boldsymbol{Q}}{\partial t} + \frac{\partial \boldsymbol{E}}{\partial x} + \frac{\partial \boldsymbol{F}}{\partial y} + H = 0 \tag{9}$$

where

$$\boldsymbol{Q} = \begin{bmatrix} \rho \\ \rho u \\ \rho v \\ \rho w \\ B_x \\ B_y \\ B_z \\ \rho e_t \end{bmatrix} \tag{10}$$

$$\boldsymbol{E} = \begin{bmatrix} \rho u \\ \rho u^2 + p + \dfrac{-B_x^2 + B_y^2 + B_z^2}{8\pi} \\ \rho uv - \dfrac{B_x B_y}{4\pi} \\ \rho uw - \dfrac{B_x B_z}{4\pi} \\ uB_x - uB_x \\ uB_y - vB_x \\ uB_z - wB_x \\ \left[\left(\rho e_t + p + \dfrac{-B_x^2 + B_y^2 + B_z^2}{8\pi} \right) u \right. \\ \left. -\dfrac{B_x}{4\pi}(vB_y + wB_z) \right] \end{bmatrix} \tag{11}$$

$$\boldsymbol{F} = \begin{bmatrix} \rho v \\ \rho uv - \dfrac{B_x B_y}{4\pi} \\ \rho v^2 + p + \dfrac{B_x^2 - B_y^2 + B_z^2}{8\pi} \\ \rho vw - \dfrac{B_y B_z}{4\pi} \\ vB_x - uB_y \\ vB_y - vB_y \\ vB_z - wB_y \\ \left[\left(\rho e_t + p + \dfrac{B_x^2 - B_y^2 + B_z^2}{8\pi} \right) v \right. \\ \left. -\dfrac{B_y}{4\pi}(uB_x + wB_z) \right] \end{bmatrix} \tag{12}$$

$$\boldsymbol{H} = \begin{bmatrix} 0 \\ \frac{B_x}{4\pi} \\ \frac{B_y}{4\pi} \\ \frac{B_z}{4\pi} \\ u \\ v \\ w \\ \frac{uB_x + vB_y + wB_z}{4\pi} \end{bmatrix} \left(\frac{\partial B_x}{\partial x} + \frac{\partial B_y}{\partial y} \right) \tag{13}$$

Two-Dimensional Governing Equations in Computational Space

The governing equation in the computational domain in a conservative form is found as the following:

$$\frac{\partial \bar{\boldsymbol{Q}}}{\partial \tau} + \frac{\partial \bar{\boldsymbol{E}}}{\partial \xi} + \frac{\partial \bar{\boldsymbol{F}}}{\partial \eta} = -\bar{H} \tag{14}$$

where

$$\bar{\boldsymbol{Q}} = \boldsymbol{Q}/J \tag{15}$$

$$\bar{\boldsymbol{E}} = (1/J)(\xi_x \boldsymbol{E} + \xi_y \boldsymbol{F}) \tag{16}$$

$$\bar{\boldsymbol{F}} = (1/J)(\eta_x \boldsymbol{E} + \eta_y \boldsymbol{F}) \tag{17}$$

$$\bar{\boldsymbol{H}} = \begin{bmatrix} 0 \\ \frac{B_x}{4\pi} \\ \frac{B_y}{4\pi} \\ \frac{B_z}{4\pi} \\ u \\ v \\ w \\ \frac{uB_x + vB_y + wB_z}{4\pi} \end{bmatrix} \left(\frac{\partial \bar{B}_x}{\partial \xi} + \frac{\partial \bar{B}_y}{\partial \eta} \right) \tag{18}$$

where

$$\bar{B}_x = (1/J)(\xi_x B_x + \xi_y B_y) \tag{19}$$

$$\bar{B}_y = (1/J)(\eta_x B_x + \eta_y B_y) \tag{20}$$

The governing equations for the two-dimensional ideal MHD flow in the computational space can be written in terms of the associated Jacobian matrices as follows:

$$\frac{\partial \bar{\boldsymbol{Q}}}{\partial \tau} + \bar{A} \frac{\partial \bar{\boldsymbol{Q}}}{\partial \xi} + \bar{B} \frac{\partial \bar{\boldsymbol{Q}}}{\partial \eta} = -\bar{H} \tag{21}$$

where

$$\bar{A} = \frac{\partial \bar{\boldsymbol{E}}}{\partial \bar{\boldsymbol{Q}}} = \xi_x A + \xi_y B \tag{22}$$

$$\bar{B} = \frac{\partial \bar{\boldsymbol{F}}}{\partial \bar{\boldsymbol{Q}}} = \eta_x A + \eta_y B \tag{23}$$

$$A = \frac{\partial \boldsymbol{E}}{\partial \boldsymbol{Q}} \tag{24}$$

$$B = \frac{\partial \boldsymbol{F}}{\partial \boldsymbol{Q}} \tag{25}$$

Eigenvalues and Eigenvectors for the System

The eigenvalues of $\bar{A}$ are determined to be

$$\lambda_{0\xi} = U \tag{26a}$$

$$\lambda_{d\xi} = U \tag{26b}$$

$$\lambda_{s\xi\pm} = U \pm V_{s\xi} \tag{26c}$$

$$\lambda_{a\xi\pm} = U \pm V_{a\xi} \tag{26d}$$

$$\lambda_{f\xi\pm} = U \pm V_{f\xi} \tag{26e}$$

where the contravarient velocities are defined as

$$U = u\xi_x + v\xi_y \tag{27}$$

$$V_{a\xi} = v_{ax}\xi_x + v_{ay}\xi_y \tag{28}$$

$$V_{f\xi}^2 = \frac{1}{2}\left[(v_a^2 + c_s^2)a_4 + \sqrt{a_4}\sqrt{(v_a^2 + c_s^2)^2 a_4 - \frac{p\gamma}{\rho^2\pi}\beta_{\xi 1}^2} \right] \tag{29}$$

$$V_{s\xi}^2 = \frac{1}{2}\left[(v_a^2 + c_s^2)a_4 - \sqrt{a_4}\sqrt{(v_a^2 + c_s^2)^2 a_4 - \frac{p\gamma}{\rho^2\pi}\beta_{\xi 1}^2} \right] \tag{30}$$

The following definitions associated with the metrics are used in the preceding expressions:

$$a_4 = \xi_x^2 + \xi_y^2 \tag{31}$$

$$\beta_{\xi 1} = B_x\xi_x + B_y\xi_y \tag{32}$$

The eigenvector matrices $\bar{X}$ and $\bar{X}^{-1}$ based on $\bar{\boldsymbol{Q}}$ are given by the following:

$$\bar{X} = [r_{0\xi}\ r_{+v_{a\xi}}\ r_{-v_{a\xi}}\ r_{+v_{f\xi}}\ r_{-v_{f\xi}}\ r_{+v_{s\xi}}\ r_{-v_{s\xi}}\ r_{d\xi}] \tag{33}$$

$$\bar{X}^{-1} = [l_{0\xi}\ l_{+v_{a\xi}}\ l_{-v_{a\xi}}\ l_{+v_{f\xi}}\ l_{-v_{f\xi}}\ l_{+v_{s\xi}}\ l_{-v_{s\xi}}\ l_{d\xi}]^T \tag{34}$$

The right and left eigenvectors are denoted by r and l, respectively, details of which are provided in Harada et al.[14]

Now, consider the Jacobian matrix $\bar{B}$. The eigenvalues are as follows:

$$\lambda_{0\eta} = V \tag{35a}$$

$$\lambda_{d\eta} = V \tag{35b}$$

$$\lambda_{s\eta\pm} = V \pm V_{s\eta} \tag{35c}$$

$$\lambda_{a\eta\pm} = V \pm V_{a\eta} \tag{35d}$$

$$\lambda_{f\eta\pm} = V \pm V_{f\eta} \tag{35e}$$

where

$$V = u\eta_x + v\eta_y \tag{36}$$

$$V_{a\eta} = v_{ax}\eta_x + v_{ay}\eta_y \tag{37}$$

$$V_{f\eta}^2 = \tfrac{1}{2}[(v_a^2 + c_s^2)b_4 + \sqrt{b_4}\sqrt{(v_a^2 + c_s^2)^2 b_4 - (p\gamma/\rho^2\pi)\beta_{\eta 1}^2}] \quad (38)$$

$$V_{s\eta}^2 = \tfrac{1}{2}[(v_a^2 + c_s^2)b_4 - \sqrt{b_4}\sqrt{(v_a^2 + c_s^2)^2 b_4 - (p\gamma/\rho^2\pi)\beta_{\eta 1}^2}] \quad (39)$$

$$b_4 = \eta_x^2 + \eta_y^2 \quad (40)$$

$$\beta_{\eta 1} = B_x\eta_x + B_y\eta_y \quad (41)$$

The eigenvector matrices $\bar{Y}$ and $\bar{Y}^{-1}$ based on $\bar{Q}$ are given by the following:

$$\bar{Y} = [r_{0\eta}\ r_{+v_{a\eta}}\ r_{-v_{a\eta}}\ r_{+v_{f\eta}}\ r_{-v_{f\eta}}\ r_{+v_{s\eta}}\ r_{-v_{s\eta}}\ r_{d\eta}] \quad (42)$$

$$\bar{Y}^{-1} = [l_{0\eta}\ l_{+v_{a\eta}}\ l_{-v_{a\eta}}\ l_{+v_{f\eta}}\ l_{-v_{f\eta}}\ l_{+v_{s\eta}}\ l_{-v_{s\eta}}\ l_{d\eta}]^T \quad (43)$$

Numerical Scheme

The modified fourth-order Runge–Kutta scheme applied to Eq. (14) yields

$$\bar{Q}_i^{(0)} = \bar{Q}_i^n \quad (44a)$$

$$\bar{Q}_{i,j}^{(1)} = \bar{Q}_{i,j}^n - \frac{\Delta\tau}{4}[L\bar{Q}^{(0)} + H^{(0)}]_{i,j} \quad (44b)$$

$$\bar{Q}_{i,j}^{(2)} = \bar{Q}_{i,j}^n - \frac{\Delta\tau}{3}[L\bar{Q}^{(1)} + \bar{H}^{(1)}]_{i,j} \quad (44c)$$

$$\bar{Q}_{i,j}^{(3)} = \bar{Q}_{i,j}^n - \frac{\Delta\tau}{2}[L\bar{Q}^{(2)} + \bar{H}^{(2)}]_{i,j} \quad (44d)$$

$$\bar{Q}_{i,j}^{n+1} = \bar{Q}_{i,j}^n - \Delta\tau[L\bar{Q}^{(3)} + \bar{H}^{(3)}]_{i,j} \quad (44e)$$

$$\bar{Q}_{i,j}^{n+1} = \bar{Q}_{i,j}^{n+1} - \frac{1}{2}\frac{\Delta\tau}{\Delta\xi}(\bar{X}_{i+1/2,j}^n\bar{\Phi}_{i+1/2,j}^n - \bar{X}_{i-1/2,j}^n\bar{\Phi}_{i-1/2,j}^n) - \frac{1}{2}\frac{\Delta\tau}{\Delta\eta}(\bar{Y}_{i,j+1/2}^n\bar{\Theta}_{i,j+1/2}^n - \bar{Y}_{i,j-1/2}^n\bar{\Theta}_{i,j-1/2}^n) \quad (44f)$$

where

$$L\bar{Q}_{i,j} = \frac{\bar{E}_{i+1,j} - \bar{E}_{i-1,j}}{2\Delta\xi} + \frac{\bar{F}_{i,j+1} - \bar{F}_{i,j-1}}{2\Delta\eta} \quad (45)$$

Three different TVD models are investigated.

TVD Models in Two Dimensions

The TVD models in two-dimensions are developed for each dimension independent of others. A typical limiter for Davis–Yee upwind TVD is given in this section. Other limiters are reported by Harada et al.[14] and the selection of limiters was based on extensive investigation of one-dimensional MHD equations.

Davis-Yee Symmetric TVD Limiters

The flux limiter functions are given as

$$\Phi_{i+1/2,j} = -\left[\frac{\Delta t}{\Delta\xi}(\lambda_{\xi_{i+1/2,j}})^2 g_{i+1/2,j} + \psi(\lambda_{\xi_{i+1/2,j}})(\alpha_{i+1/2,j} - g_{i+1/2,j})\right] \quad (46a)$$

$$\Phi_{i-1/2,j} = -\left[\frac{\Delta t}{\Delta\xi}(\lambda_{\xi_{i-1/2,j}})^2 g_{i-1/2,j} + \psi(\lambda_{\xi_{i-1/2,j}})(\alpha_{i-1/2,j} - g_{i-1/2,j})\right] \quad (46b)$$

$$\Theta_{i,j+1/2} = -\left[\frac{\Delta t}{\Delta\eta}(\lambda_{\eta_{i,j+1/2}})^2 h_{i,j+1/2} + \psi(\lambda_{\eta_{i,j+1/2}})(\beta_{i,j+1/2} - h_{i,j+1/2})\right] \quad (47a)$$

$$\Theta_{i,j-1/2} = -\left[\frac{\Delta t}{\Delta\eta}(\lambda_{\eta_{i,j-1/2}})^2 h_{i,j-1/2} + \psi(\lambda_{\eta_{i,j-1/2}})(\beta_{i,j-1/2} - h_{i,j-1/2})\right] \quad (47b)$$

The entropy correction, ψ, is given as

$$\psi(y) = \begin{cases} |y|, & |y| \geq \varepsilon \\ \dfrac{(y^2 + \varepsilon^2)}{2\varepsilon}, & |y| \leq \varepsilon \end{cases}, \qquad 0 < \varepsilon \leq 0.125 \quad (48)$$

The following limiters are selected

$$g_{i+1/2,j} = \text{minmod}\{2\alpha_{i-1/2,j},\ 2\alpha_{i+1/2,j},\ 2\alpha_{i+3/2,j},\ \tfrac{1}{2}(\alpha_{i-1/2,j} + \alpha_{i+3/2,j})\} \quad (49)$$

$$h_{i,j+1/2} = \text{minmod}\{2\beta_{i,j-1/2},\ 2\beta_{i,j+1/2},\ 2\beta_{i,j+3/2},\ \tfrac{1}{2}(\beta_{i,j-1/2} + \beta_{i,j+3/2})\} \quad (50)$$

Results and Discussions

The accuracy and robustness of the numerical scheme for two-dimensional applications are demonstrated in this section. A supersonic flow within a channel including compression and expansion corners is used for this purpose. Solutions are obtained for six different cases, each under the influence of a different magnetic field and freestream Mach number. The freestream pressure is 100 kPa, and the freestream temperature is 300 K. The specified magnetic fields and Mach numbers are provided in Table 1.

Based on the investigation of the one-dimensional problem reported by Harada et al.,[14] the Davis–Yee symmetric TVD model with limiters [Eqs. (49) and (50)] is selected as the added dissipation mechanism to the numerical scheme. The typical domain is shown in Fig. 1, where the specific dimensions for the applications in this section are $L_1 = 10$ cm, $L_2 = 20$ cm, $L_3 = 40$ cm, $L_4 = 28$ cm, $L_5 = 42$ cm, $H_1 = 20$ cm, and $\delta = 10$ deg. The grid distribution around the boundary is set as $I_1 = 2_1$, $I_2 = 91$, $I_4 = 61$, $IM = 241$, and $JM = 131$. The grid points are clustered at the compression and expansion corners and at the expected locations of shock reflections.

Computations are initialized by specification of inflow conditions over the domain. A local time stepping is used to obtain a steady-state solution. Figure 2 shows typical convergence histories. The specified Courant–Friedrichs–Lewy number for all cases is 0.2. The steady-state solutions are reached after

Table 1 Specification of Mach number and magnetic field

Case	M_∞	$\bar{B}$
1	2.0	$0i + 0j$
2	2.0	$100\sqrt{4\pi}i + 200\sqrt{4\pi}j$
3	2.0	$100\sqrt{4\pi}i - 200\sqrt{4\pi}j$
4	3.0	$0i + 0j$
5	3.0	$100\sqrt{4\pi}i + 200\sqrt{4\pi}j$
6	3.0	$100\sqrt{4\pi}i - 200\sqrt{4\pi}j$

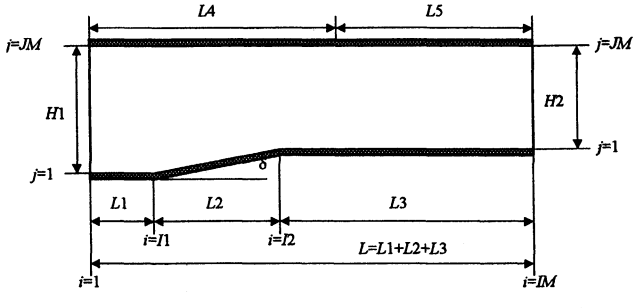

Fig. 1 Illustration of the physical domain and its nomenclature.

8820, 14,471, and 10,367 for cases 1, 2, and 3, respectively. The convergence criterion for all cases is set at

$$\text{Conv} = \sum_{\substack{i=2 \\ j=2}}^{\substack{j=JMM1 \\ i=IMM1}} (p^{n+1} - p^n) \leq 0.1$$

The pressure contours illustrating the formation of oblique shock, expansion wave, and their interaction and reflection are shown in Figs. 3–5 for cases 1–3. With a magnetic field corresponding to cases 2 and 3 being activated, the pressure contours include additional wave formations as shown in Figs. 4 and 5. The pressure distributions at the j location of 1 (lower surface), 20, 50, and 110 are shown in Figs. 6–8, respectively. A comparison with the analytical solution is also shown in Fig. 6. A secondary compression wave is generated after the oblique shock and originated at the compression corner as seen in Fig. 4 and the accompanying pressure rise in Fig. 6. Further downstream at the expansion corner a secondary expansion wave is generated just behind the primary expansion wave. This secondary wave is specified as an expansion wave caused by pressure drop, as evident in Fig. 6. The reflection of the oblique shock from the surface is accompanied with an expansion wave at both the lower and upper surfaces. The associated drop in pressure near the upper surface is shown in Fig. 8. This reflected wave is similar and can be interpreted as a compound wave identified in the one-dimensional magnetic shock-tube problem. When the magnetic field is modified to that of case 3, the secondary waves become much weaker. In fact, no secondary wave is observed at the compression or the expansion corners, and the reflected oblique shock is accompanied with a very weak expansion wave. It is interesting to note that the maximum pressure rise downstream of the reflected waves is smaller when the magnetic field is activated.

The pressure contours illustrating the formation of oblique shock, expansion wave, and their interaction and reflection for cases 5 and 6 are shown in Figs. 9 and 10. The pressure and

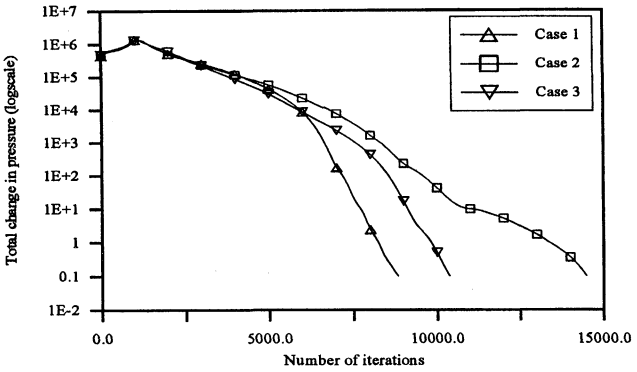

Fig. 2 Comparison of convergence histories for $M_\infty = 2.0$.

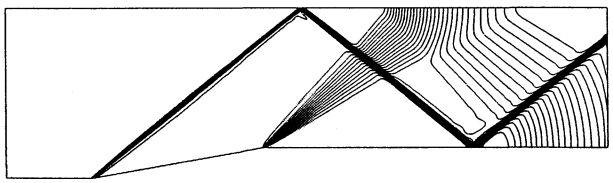

Fig. 3 Pressure contours for case 1.

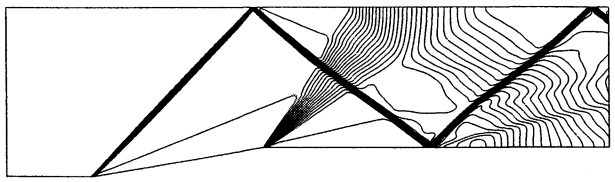

Fig. 4 Pressure contours for case 2.

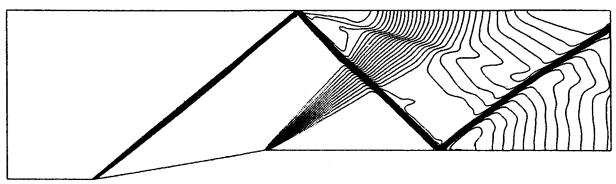

Fig. 5 Pressure contours for case 3.

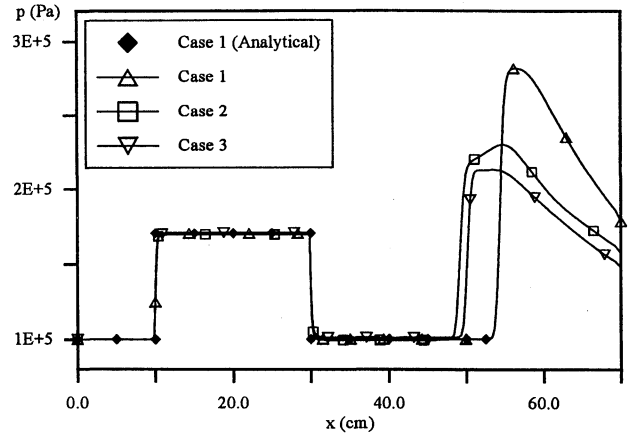

Fig. 6 Comparison of the pressure distributions on the lower surface for $M_\infty = 2.0$.

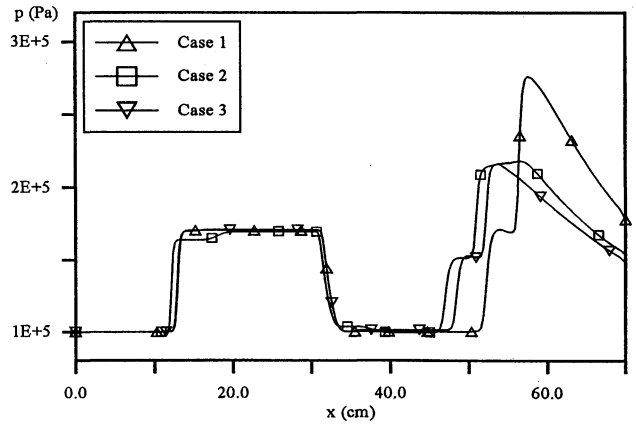

Fig. 7 Comparison of the pressure distributions at $j = 20$ for $M_\infty = 2.0$.

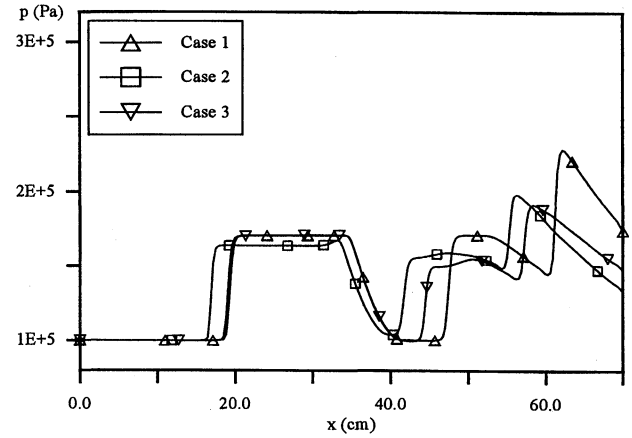

Fig. 8 Comparison of the pressure distributions at $j = 50$ for $M_\infty = 2.0$.

density distributions at the j location of 1 (lower surface), 20, 50, and 110 are shown in Figs. 11–14, respectively. With a magnetic field corresponding to case 5 being activated, the pressure contours include additional wave formations as shown in Fig. 9, which were also observed for $M_\infty = 2.0$. A comparison with analytical solution is also included in Fig. 11. As observed for case 2 a secondary compression wave is also generated after the oblique shock originated at the compression corner for case 5 as seen in Fig. 9. The accompanying pressure rise is illustrated in Fig. 12. However, note that the pressure rise is larger than that of case 2. In addition, a secondary expansion wave at the expansion corner that was observed for case 2 is also generated for case 5 just behind the primary expansion wave. This secondary wave is specified as an expansion wave similar to that of case 2 as evident in Fig. 12. It is interesting to note that the pressure drop is almost the same as that of case 2, whereas the pressure rise at the secondary compression wave at the compression corner is clearly larger than that of case 2. The reflection of oblique shock from the surface is accompanied with a wave at the upper surface as shown in Fig. 10. This weak wave is classified as an expansion wave; however, the associated drop in pressure is not clearly observed in Fig. 14. The secondary compression and expansion waves at the corners do not appear for case 6. Note that similar observation was made for case 3. However, the secondary wave after reflection persist in cases 3 and 6.

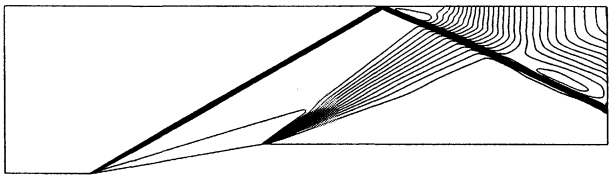

Fig. 9 Pressure contours for case 5.

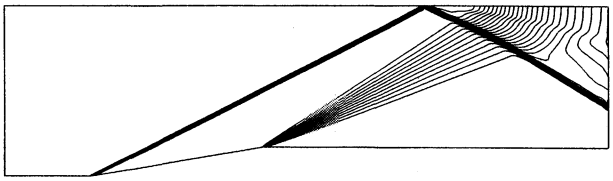

Fig. 10 Pressure contours for case 6.

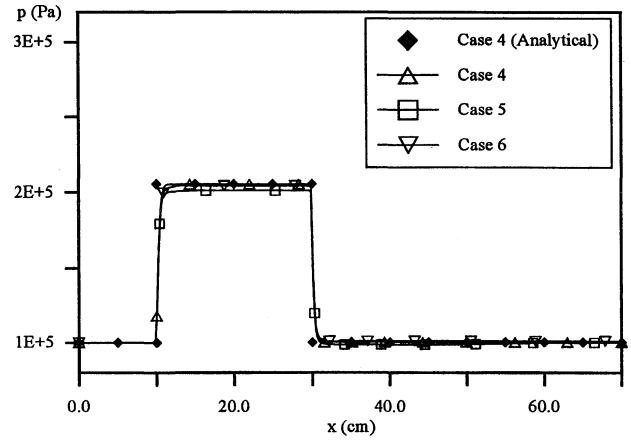

Fig. 11 Comparison of the pressure distributions on the lower surface for $M_\infty = 3.0$.

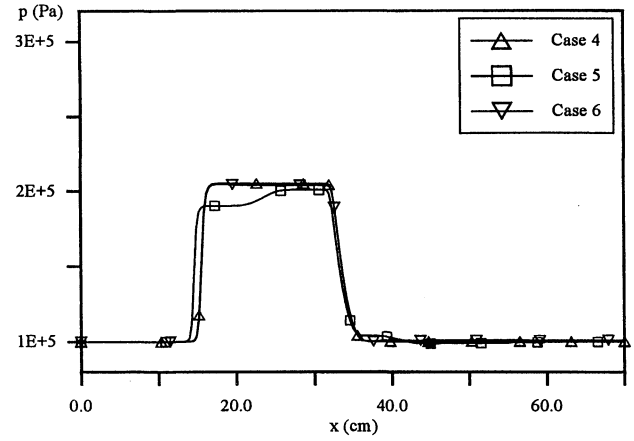

Fig. 12 Comparison of the pressure distributions at $j = 20$ for $M_\infty = 3.0$.

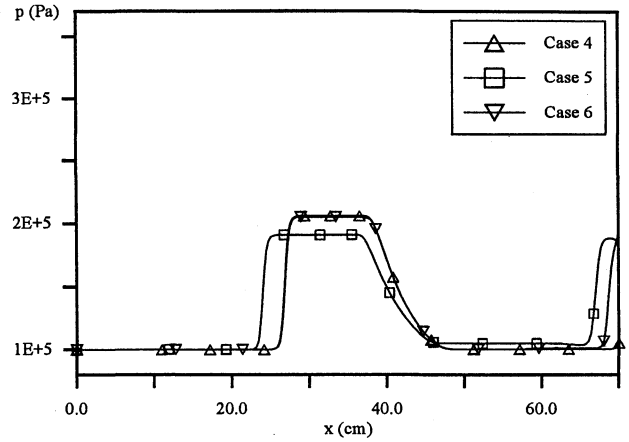

Fig. 13 Comparison of the pressure distributions at $j = 50$ for $M_\infty = 3.0$.

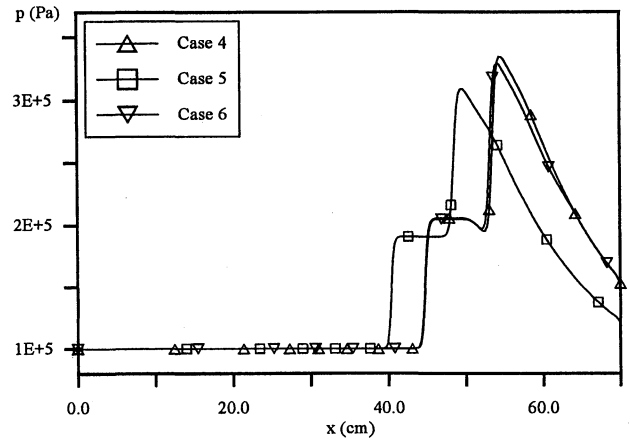

Fig. 14 Comparison of the pressure distributions at $j = 110$ for $M_\infty = 3.0$.

Conclusions

A fourth-order modified Runge–Kutta scheme is used to solve the fluid dynamics/magnetic field interaction phenomenon. TVD models have been implemented as a dissipation mechanism in the solution procedure. A set of new eigenvectors that are required in the implementation of various TVD models have been developed. The solutions are compared to analytical solutions when available. The scheme is shown to be accurate, efficient, and relatively robust.

A supersonic two-dimensional channel flow that includes a compression corner, an expansion corner, shock/expansion interaction, and wave reflections is investigated. A secondary set of compression and expansion waves are identified when the fluid is under the influence of the magnetic field. The wave reflection is also influenced by the magnetic field, and the shock reflection is in the form of a compound wave. It is

evident that the wave strength and pattern are influenced by the imposed magnetic field.

Acknowledgment

This work was partially supported by the Kansas Center for Advanced Scientific Computing sponsored by the NSF EPSCoR/K*STAR program.

References

[1]Godunov, S. K., "A Finite Difference Method for the Numerical Computations of Discontinuous Solutions of the Equations of Fluid Dynamics," *Math. Sbornik.*, Vol. 47, 1959, pp. 271–306.

[2]Roe, P. L., "Approximate Riemann Solvers, Parameter Vectors, and Difference Schemes," *Journal of Computational Physics*, Vol. 43, 1981, pp. 357–372.

[3]Yee, H. C., "A Class of High-Resolution Explicit and Implicit Shock-Capturing Methods," NASA TM 101088, Feb. 1989.

[4]Steger, J. L., and Warming, R. F., "Flux Vector Splitting of the Inviscid Gasdynamic Equations with Application to Finite-Difference Methods," *Journal of Computational Physics*, Vol. 40, 1981, pp. 263–293.

[5]Van Leer, B., "Flux Vector Splitting for the Euler Equations," *Lecture Notes in Physics 170, 8th International Conference on Numerical Methods in Fluid Dynamics*, 1982, pp. 501–512.

[6]Liou, M., and Steffen, J., Jr., "A New Flux Splitting Scheme," NASA TM 104404, May 1991.

[7]Halt, D. W., and Agarwal, R. K., "A Novel Algorithm for the Solution of Complessible Euler Equations in Wave/Particle Split (WPS) Form," *Proceedings of the 11th AIAA Computational Fluid Dynamics Conference* (Orlando, FL), AIAA, Washington, DC, 1993.

[8]Brio, M., and Wu, C. C., "An Upwind Differencing Scheme for the Equations of Ideal Magnetohydrodynamics," *Journal of Computational Physics*, Vol. 75, 1988, pp. 400–422.

[9]Dai, W., and Woodward, P. R., "An Approximate Riemann Solver in Magnetohydrodynamics," Univ. of Minnesota Supercomputer Inst. Research, Rept. 91/329, Minneapolis, MN, Dec. 1991.

[10]Dai, W., and Woodward, P. R., "Extension of the Piecewise Parabolic Method to Multidimensional Ideal Magnetohydrodynamics," *Journal of Computational Physics*, Vol. 115, 1994, pp. 485–514.

[11]Dai, W., and Woodward, P. R., "A Simple Riemann Solver and High-Order Godunov Schemes for Hyperbolic Systems of Conservation Laws," *Journal of Computational Physics*, Vol. 121, 1995, pp. 51–65.

[12]Zachary, A. L., and Colella, P., "A Higher-Order Godunov Method for the Equations of Ideal Magnetohydrodynamics," *Journal of Computational Physics*, Vol. 99, 1992, pp. 341–347.

[13]Powell, K. G., "An Approximate Riemann Solver for Magnetohydrodynamics (That Works in More Than One Dimension)," NASA CR 194902, Inst. for Computer Applications in Science and Engineering Rept. 94-24, April 1994.

[14]Harada, S., Augustinus, J., Hoffmann, K. A., and Agarwal, R. K., "Development of a Modified Runge-Kutta Scheme with TVD Limiters for the Ideal 1-D MHD Equations," AIAA Paper 97-2090, June 1997.